


Research Article

The Seepage-Destruction Mechanism of Water Inrush Channel of Sandstone Fault Filling Using the EDEM-Fluent Method

Wenya Cai,¹ Yan Wang,² Fujun He,² Pengyuan Zhang,² and Shuo Sun³ 

¹Beijing Guodaotong Highway Design & Research Institute Co., Ltd, Beijing 100055, China

²Beijing Uni.-Construction Group Co., Ltd, Beijing 101200, China

³School of Civil Engineering, Beijing Jiaotong University, Beijing 100044, China

Correspondence should be addressed to Shuo Sun; 20125912@bjtu.edu.cn

Received 15 August 2022; Accepted 9 September 2022; Published 5 October 2022

Academic Editor: Chao Zou

Copyright © 2022 Wenya Cai et al. This is an open access article distributed under the Creative Commons Attribution License, which permits unrestricted use, distribution, and reproduction in any medium, provided the original work is properly cited.

By the EDEM-Fluent coupling calculation method, the formation mechanism of the seepage failure water inrush channel and the migration of particles in the sandstone fault filling body are studied. Under the condition of variable hydraulic gradient, the whole seepage process can be divided into three stages: slow seepage stage, sudden seepage stage, and stable seepage stage. In the stage of slow seepage, the mass of lost particles is small. In the stage of sudden seepage, particles are lost on a large scale. In the stable seepage stage, the model is basically in a stable state. During the seepage process, the particles in the outlet zone will move before the particles in the inlet zone under the action of the seepage force. The overall movement trend of particles can be predicted, while the movement trajectory of a single particle is irregular. The change trend of the contact quantity between particles is basically consistent with the change in the quality of the lost particles. Moreover, the change in the contact quantity of particles is caused by the loss of the filler particles.

1. Introduction

During the construction of mountain tunnels, geological disasters of different degrees will be suffered and water inrush is common [1–3]. Its frequent occurrence and harmfulness bring great resistance to tunnel survey, design, and construction [4–8]. When crossing karst caves and fault fracture zones under water-rich conditions, karst-type water inrush usually occurs [9–11]. Besides, the fissure type water inrush occurs under the influence of water storage structure and rainfall, and the water inrush pressure even exceeds 2 MPa [12–14]. Fault-type water inrush occurred during the excavation of two regional rock fault planes under severe weathering conditions, and the water flow was very huge, even reaching 1800 m³/h [15].

With the increasing demand for safety in the process of tunnel construction, a series of empirical standards and analysis models are proposed for the occurrence mechanism of water inrush, the prediction of water inrush volume, water inrush location, and water inrush characteristics. Guo et al. [16] used UDEC software based on the discrete element

method, which was combined with laboratory tests, and analyzed the occurrence mechanism of water inrush in karst tunnels from macroperspectives and microperspectives. It was clarified that the secondary stress redistribution of surrounding rock and karst water pressure with a high head easily caused water inrush in karst tunnels. Using the finite difference program, Jiang et al. [17] calculated the instantaneous and stable water inflow during deep and long tunnel excavation in bedrock fissure aquifers and established a reliable and practical hydrogeological model. Based on the finite element method, Li [18] explored the seepage characteristics of groundwater and identified the location of inrush water as the vault and the arch waist on both sides and proposed the cement-water glass double slurry water-blocking measures. Zhao and Yang [19] analyzed the characteristics of water inflow when the tunnel passes through the fault fracture zone. When the tunnel collapses, the water inflow pressure will drop sharply and the existence of surface water will increase the water inflow and grouting thickness of the tunnel.

However, the traditional analysis method cannot be suitable for the complex fault fracture zone conditions, and the simulation of fluid movement is also relatively effective. The SPH method can be applied to solve complex fluid dynamics [20]. Bai et al. [21] proposed an SPH-FDM boundary method to analyze heat transfer in homogeneous media with discontinuous interfaces [22]. It should be noted that hydrogeological conditions are not the only determinant of water inrush type and seepage path [5, 23–25]. Bai et al. [26, 27] established a nonlinear coupled transport equation of water movement driven by temperature in unsaturated soil. The water distribution under the action of the temperature gradient is uneven, which verified the hysteresis effect of water movement caused by the thermal cycle. A thermo-mechanical composition model is established for the particle rearrangement problem caused by the thermodynamics of porous granular materials, which can be used to describe the path problem in the process of water migration [28]. Bai et al. [29] explored the dynamic characteristics of suspended particles in porous media under variable temperature and proposed that water viscosity, adsorption effect, electric double layer effect, and particle kinetic energy will all affect particle motion.

The Zhaitang Mountain Tunnel of the G109 expressway has sandstone geological conditions. The fault fracture zone will be exposed during the construction process, the fault runs through the Zhaitang Tunnel and Zhaitang reservoir, and the shortest horizontal distance is only 320 meters. Based on the geotechnical dominant surface theory, it belongs to the dangerous water-conducting section [30, 31]. With the tunnel excavation, the permeability coefficient of the fault fracture zone increases and the water source in the Zhaitang reservoir may carry the filling material in the fault to gush water into the tunnel along the fault fracture zone, thus forming a relatively through seepage channel, which is prone to seepage damage type water inrush of the filling body [9, 32–35]. Based on the DEM-CFD coupling calculation method, Zhou et al. [36] used a $100\text{ mm} \times 50\text{ mm} \times 100\text{ mm}$ rock mass model to simulate the engineering scale water inrush process with a real time of 1.8 s, showing the formation and expansion process of the dominant channel of water inrush. Through the self-designed test system, Wang et al. [37] made samples with a diameter of 100 mm and a height of 500 mm to qualitatively study the mechanism of water inrush caused by the migration of fault-filling particles. Xu et al. [38] used PFC3D software to build a fault fractured rock mass model with a diameter of 60 mm and a height of 120 mm and simulated the disaster process of water inrush in a microscopic view. Through the laboratory test method, Chen and Lyu [39] made a $30\text{ mm} \times 30\text{ mm} \times 110\text{ mm}$ sample of the broken rock mass to discuss the change law and influencing factors of the particle migration on the hydraulic properties of the sandstone in the fault fracture zone during the occurrence of water inrush.

During the formation of seepage failure type water inrush channel in sandstone fault filling body, there is the interaction between particle phase and fluid phase. Not only the independent migration and stress of solid particles and

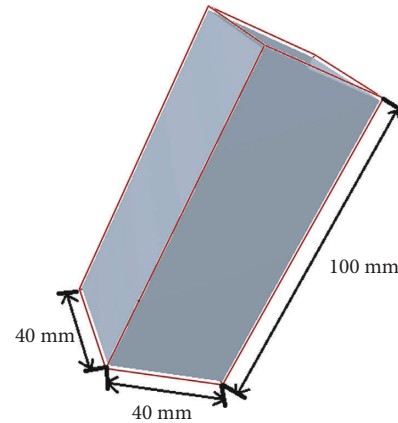


FIGURE 1: Geometric model.

fluid but also the exchange of energy, momentum, and mass between solid particles and fluid should be considered. Based on the fluid-solid coupling theory, this paper adopts the coupling method of discrete element software EDEM 2018 and computational fluid dynamics software Fluent 18.0, which is more accurate than the traditional method (i.e., PFC method), to establish a small-scale broken sandstone model and carry out three-dimensional numerical simulation. The formation mechanism of the water inrush channel and the migration law of particles in the seepage process are explored.

2. Modeling of Broken Sandstone

2.1. EDEM Geometric Model. The fault fracture zone of tunnel excavation is a dangerous section for water diversion. Using EDEM software and the discrete element method, the model of broken sandstone inside the fault is established, which is expressed by several particle combinations. However, it is difficult to establish a stratum model which is equivalent to the actual engineering size in the process of numerical simulation due to the limitation of computer capabilities. Therefore, combined with actual working conditions, a $40\text{ mm} \times 40\text{ mm} \times 100\text{ mm}$ rectangular broken sandstone millimeter scale model [40, 41] with an initial porosity of 18.27% was studied to discuss the formation mechanism of seepage failure type water inrush channel of sandstone fault backfill under the action of reservoir seepage force.

As shown in Figure 1, the dark gray area is the geometric area where particles are generated, and the red border is the calculation domain. That is, if the particle movement exceeds the calculation domain, it will be deleted automatically. The highest water level of the Zhaitang reservoir is lower than the design elevation of the tunnel, so the flow in this model is seepage from bottom to top. The six faces of the broken sandstone model are all walls. The bottom and top faces are, respectively, set as fluid inlets and outlets. The physical properties of the surrounding walls are consistent with those of the sandstone, and none of them has water permeability. The top face of the model was deleted so that the particles inside the model can gush outward under the action of single

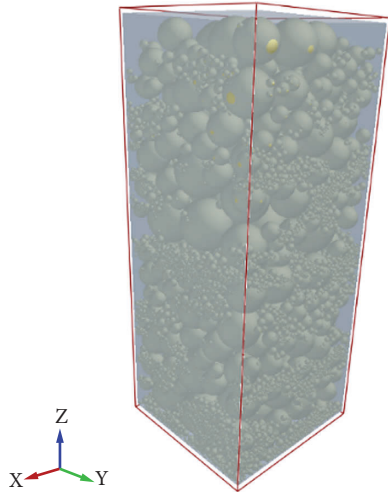


FIGURE 2: Sandstone model generated by EDEM.

bottom-up water seepage. Among them, the initial hydraulic gradient at the inlet is 0.1, increasing by 0.1 every 0.1 s in a stepped manner, and the fluid outlet pressure is constant at 0.

Broken rock mass is considered to be composed of rock mass skeleton and filling medium. In combination with the actual conditions of the tunnel, two particles with different particle size ranges are used to represent the skeleton particles (2–15 mm) and filling particles (0.25–2 mm), respectively, to simulate the broken sandstone. The ratio of filling particles to skeleton particles is 1:3, all particle shapes are simplified to spheres, and they are rigid elements that cannot be deformed. EDEM software based on the discrete element principle is used to generate broken sandstone particles. The particle sizes of filling particles and skeleton particles are randomly generated within their desirable range, and a total of 18985 particles were generated. Figure 2 shows the broken sandstone model generated by EDEM with a gravity of 9.8 KN/m^3 and a negative direction along the Z axis.

It should be noted that fault fractured rock mass is formed by bonding a series of discontinuous particles, and different particle contact models will produce different contact forces. Based on this, the contact between skeleton particles is set as Hertz–Mindlin with the bonding model to simulate the adhesion between particles. Skeleton particles with certain adhesion constitute a skeleton network. Once the adhesion between particles is destroyed, the particles will change to Hertz–Mindlin (No Slip) model when they contact again. According to field measurement and theoretical analysis, the physical parameters of particles are shown in Table 1.

Due to the difference between the mesh generation in EDEM software and the mesh size of fluid computing, when using EDEM-Fluent for coupling calculation, it is necessary to divide the mesh of EDEM and fluid computing, respectively. The mesh size of EDEM is directly related to the minimum particle size, which is usually about twice the minimum particle radius. The selected EDEM grid size is 2.5 times of the minimum particle radius, and the minimum radius of generated particles is 0.125 mm. Hence, the grid size is 0.3125 mm, including a total of 5611647 grids. To

TABLE 1: Particle parameter setting.

Particle parameter	Numerical value
Poisson's ratio	0.2
Density	$2.08 \times 10^3 \text{ kg/m}^3$
Modulus of elasticity	$3.3e + 10 \text{ Pa}$
Static friction coefficient	0.5
Rolling friction coefficient	0.05
Filling particle size	0.25–2 mm
Skeleton particle size	2–15 mm
Particle shape	Sphere
Model size	40 mm × 40 mm × 100 mm
Skeleton particle contact model	Hertz–Mindlin with bonding model

ensure the grid quality and the accuracy of calculation results, a single fluid calculation grid must contain at least three solid particles, and the size of the fluent fluid grid is $10 \text{ mm} \times 10 \text{ mm} \times 10 \text{ mm}$, including a total of 160 fluid computing grid cells.

2.2. EDEM Calculation Principle. In the discrete element method, the particle motion follows Newton's second law of motion [42], and the interaction between particles is a transient process. Within a sufficiently small time step, it can be assumed that the velocity and acceleration of a single particle are fixed values and only the particles or boundaries in direct contact with it play a role without being affected by the indirect action of other particles. The basic equation of motion for a single particle is as follows:

$$m \frac{d^2 u}{dt^2} + f_d + f_c + f = 0, \quad (1)$$

$$I \frac{d^2 \theta}{dt^2} = \sum r_c f_c,$$

where m is the particle mass, u is the linear displacement, θ is the angular displacement, f_d , f_c , and f are the damping force contact force and volume force on the particles, respectively, I is the moment of inertia, and r_c is the force arm of the contact force on the particles.

During EDEM calculation, the particle and boundary position will be obtained. Taking the relative displacement between particles as the basic physical variable, the normal force and tangential force of particles will be obtained according to the relationship between force and displacement in the contact model, so as to obtain the resultant force and resultant moment. Then, the physical quantities such as displacement, velocity, and acceleration of particles will be calculated according to Newton's second law of motion, and the continuous cycle calculation will be carried out. Fluent calculation ensures that the fluid motion follows the continuity equation and momentum conservation equation.

3. Numerical Simulation and Discussion

3.1. Particle Movement. The total duration of seepage failure of the simulated sandstone fault filling body is 1 s, the time step of EDEM is set as 1×10^{-7} s, and the data saving interval

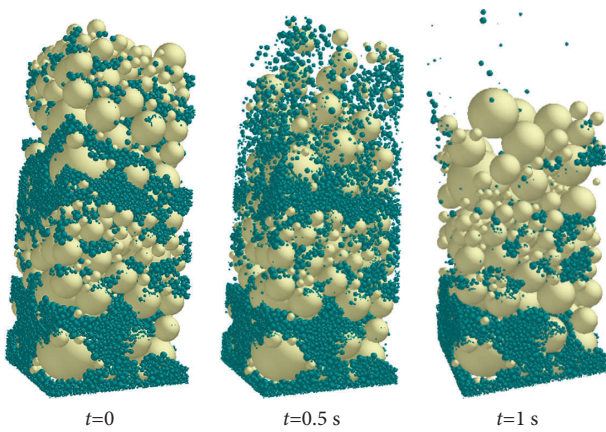


FIGURE 3: Particle movement at different times.

is 0.01 s. The time step ratio of EDEM and Fluent is 1 : 100, and the time interval ratio of data saving is 1 : 10. Within the calculation time, EDEM needs to calculate 10 million steps in total and Fluent needs to calculate 100000 steps in total.

Figure 3 shows the particle state in the model when $t = 0$, $t = 0.5$ and $t = 1.0$ s in the seepage process [22]. The dark green particles are filling particles and the yellow-green particles are skeleton particles. Different time points correspond to different hydraulic gradients [27]. By observing the particle state at different time points, based on the loss speed and amount of particles, the movement law of particles under the action of fluid seepage force with gradient increase can be obtained.

When the seepage force is small, the filling particles in the outlet area along the direction of seepage force and some skeleton particles outside the skeleton network will gush out before the particles in the inlet area [43], and the particle position in the inlet area has no obvious change and is in a stable state. With the increase of hydraulic gradient, the resultant force of fluid drag force, gravity, and indirect contact force of particles in the middle section occurs gradually upward and the contact relationship between particles also changes. The flow will carry a large number of filling particles and some small skeleton particles from the high water pressure to the low water pressure area. At this stage, the filling particles gush out on a large scale, some small skeleton particles will also be lost, and the large skeleton particles will move unsteadily with the change of contact relationship. As most of the filling particles have gushed out, the remaining filling particles will gradually stabilize, but there are still a small part of filling particles and small skeleton particles slowly gushing out. Due to the change of the contact relationship between particles, the particles moving from the middle and lower part to the outlet area under the action of seepage force will also gush out. The filling particles in the inlet area cannot gush out because of the large skeleton particles and form a stable structure with the remaining skeleton particles.

When $t = 1$ s, the seepage simulation process ends, and most of the filling particles and a small part of the skeleton particles have gushed out, which further increases the porosity, permeability coefficient, and water velocity of the

fault fracture zone, forming a relatively smooth water inrush channel. In addition, the loss of particles is obviously nonuniform. Although the particles migrate first in the outlet area, the particles do not gush out layer by layer, indicating that the water velocity in the particle pores is different in the same horizontal plane, and the seepage path is irregular [44]. However, under the action of the drag force of the water flow, it drives the filling particles and some skeleton particles to gush out, thus forming a relatively smooth water inrush channel.

According to the motion law of a single particle, the motion trajectories of three particles in the outlet area, the middle section, and the inlet area are randomly selected (Figure 4). In the process of gushing, a single particle moves under the combined action of gravity, water drag force, normal contact force, and tangential contact force between different particles. The upward migration and gushing of filling particles and some small skeleton particles along the direction of seepage force need to pass through the pores between skeleton networks. The particle sizes of single particles randomly selected may be different, and the gravity of particles with different sizes is different [45, 46]. Because the pore size and the flow velocity and direction are different between the skeleton particles, the size and direction of the flow drag force on different particles are different. The contact relationship between a single particle and other particles is not exactly the same [47–49], and the sizes and directions of normal, tangential, and angular velocities of particles affected by water flow are also different. Similarly, there are differences in the moment of inertia of particles with different particle sizes [50]. Therefore, the sizes and directions of normal and tangential contact forces on a single particle at different times are different, which leads to different resultant forces of a single particle under the action of water flow.

Actually, the movement of particles is irregular and will not strictly follow the action direction of seepage force. For example, the single particle movement tracks in the middle section selected in Figure 4 move downward first and then upward. Figure 5 more intuitively shows the trajectory of the particle, in which the purple particle is the characteristic particle, the dark green particle is the filling particle, and the yellow-green particle is the skeleton particle. The motion track of the characteristic particle starts because the particle is a skeleton particle free from the skeleton network. Under the action of initial water pressure, the force of seepage force on the skeleton particle is not enough to make it move upward and gush out, but the drag force of water flow can carry the filling particles around the particle upward, thus changing the contact relationship between the particle and other filling particles. With the increase of seepage force, the surrounding filling particles continuously gush out and the contact force between particles decreases. The gravity of the characteristic particles gradually plays a leading role in the resultant force, and the resultant force direction of the particles is gradually downward, so the particles move downward first. As the seepage force continues to increase, the drag force of the water flow on the characteristic particles continues to increase and the resultant force on the particles gradually moves upward. The drag force begins to dominate

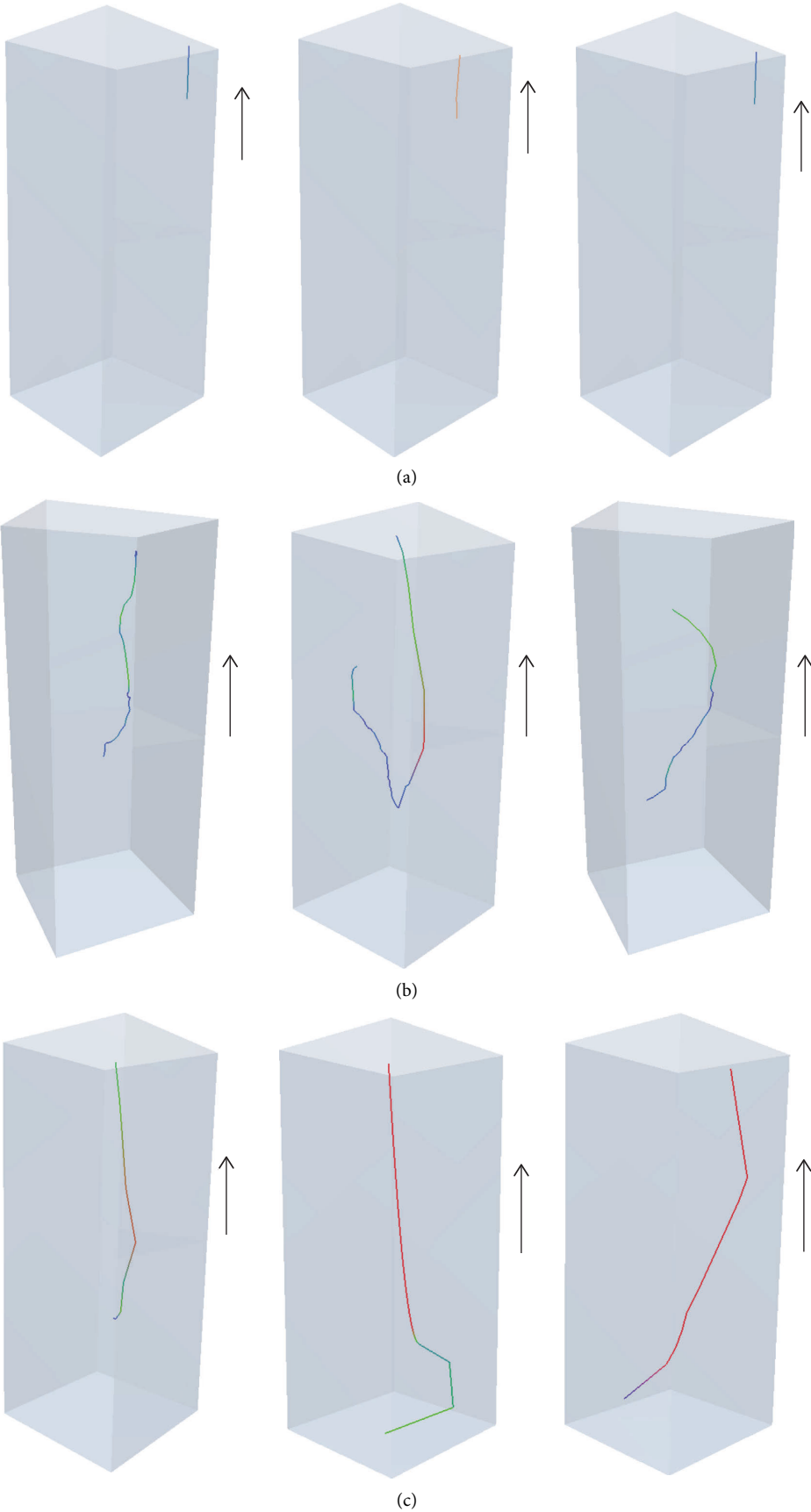


FIGURE 4: Particle trajectory. (a) Outlet area particles, (b) middle section particles, and (c) inlet area particles.

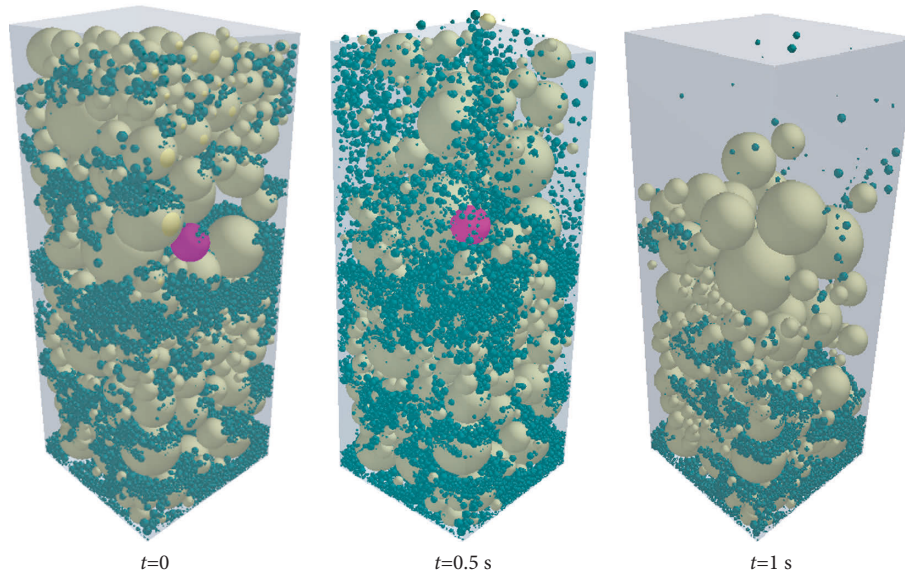


FIGURE 5: The trajectory of particle 1.

the movement direction of the particles, and the particles move upward.

To clarify the influence of the particle indirect contact force on the motion trajectory of the characteristic particle, the change of the particle indirect contact force of particle 1 in the whole seepage process is output in the EDEM postprocessing (Figure 6). Within 0–0.2 s, the filling particles begin to move under the action of the drag force of water flow, and the contact relationship between the characteristic particles and the surrounding filling particles changes, so the contact force on the particles begins to decrease gradually. At this time, particle 1 does not move, and at the same time, the pores around the particle increase. After 0.2 s, gravity plays a leading role, and the characteristic particles begin to move downward, but the drag force of the water flow on the particles increases with the increase of the hydraulic gradient, and the particles begin to move upward until they gush out of the channel at 0.6 s. During the movement of the particle, it is subjected to a short and slight contact force at some time because the particle collides with other particles during the movement.

The trajectory of a single particle is also different in the middle section shown (Figure 4). In the process of particle emission, some particles do not move upward along the direction of seepage force but remain stationary after a period of upward movement until the end of seepage. The reason for the particle trajectory is that at the beginning, the filling particles move upward under the action of the water drag force, get stuck between the skeleton network formed by the large skeleton particles after a certain distance, and then reach a stable state. Because the characteristic particle is located inside the model and it is difficult to observe directly, other particles are hidden and only the characteristic particle is displayed (Figure 7). The characteristic particle moves upward slowly under the initial water pressure, and it moves violently at 0.8 s and finally stops the upward trend.

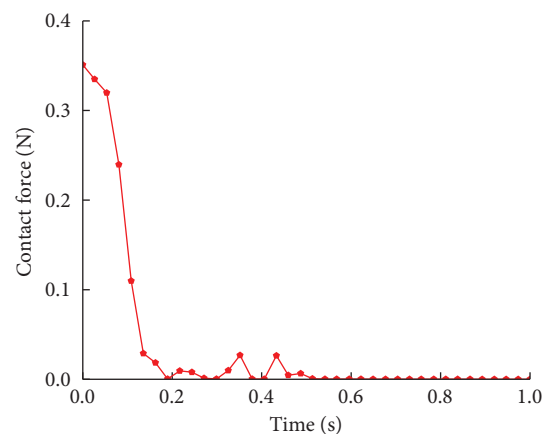


FIGURE 6: The contact force variation of characteristic particle 1.

3.2. Mass Change of Lost Particles. To explore the particle emission during the seepage process, using the post-processing function of EDEM software, the change of residual particle mass with time is shown in Figure 8, which can directly reflect the particle loss speed and mutation point at different time points and the particle emission in a certain period of time. Figure 9 shows the variation of lost particle mass with time during the whole seepage process. It can be seen that within 0–0.3 s, the slope of the curve is relatively flat, and the particle loss speed is relatively slow. At 0.3 s, the slope of the curve increases sharply, the particles begin to lose on a large scale and the particle loss speed and amount increase. After 0.8 s, the curve slope tends to be flat again, the particle loss speed gradually decreases, and the particle loss quality tends to be stable.

The particle loss process can be divided into three stages. In the first stage (slow seepage stage, 0–0.3 s), the particle loss mass in this stage is 5.0 g, accounting for 5.41% of the total mass loss in the whole seepage process. The initial hydraulic

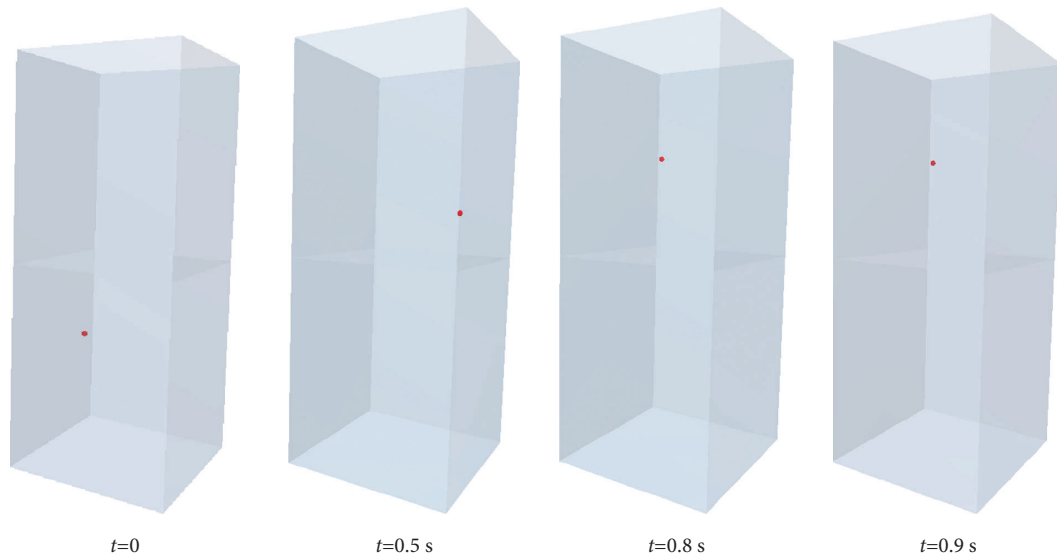


FIGURE 7: Characteristic particle trajectory.

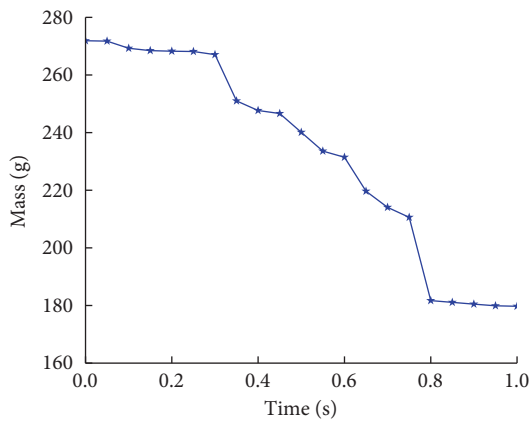


FIGURE 8: Broken line diagram of residual mass variation with numerical simulation time.

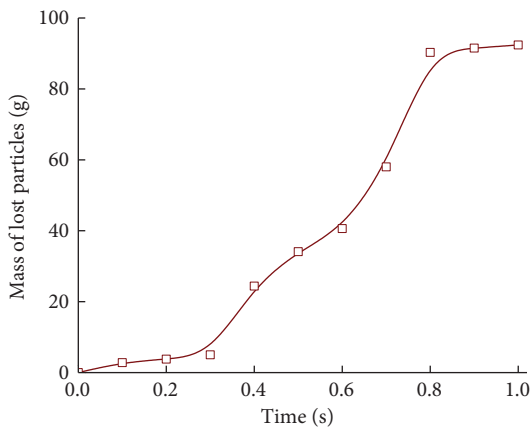


FIGURE 9: Variation curve of lost particle mass with time.

gradient is 0.1, the drag capacity of the flow is low, the filling particles in the outlet area will move upward slowly, and the skeleton particles will not move because of their own gravity and the large contact force between the particles. The loss

mass of particles in 0–0.1 s is 2.8 g, accounting for 56% of the total mass of particles lost in the slow seepage stage. This is because the upward movement of particles in the outlet area is not hindered by other particles. After this part of the particles gushes out, the rest of the filling particles and some of the small skeleton particles free from the skeleton network begin to move upward. However, due to the drag force of water flow, the outflow velocity and outflow volume of particles are relatively small. In practical engineering, the seepage volume is small, and the water flow is relatively clear. This stage is the best time to take corresponding measures. Grouting and water plugging at appropriate positions can avoid the formation of water inrush channels. In the second stage (sudden seepage stage, 0.3 s–0.8 s), the critical hydraulic gradient corresponding to the starting point is 0.4 and the total mass loss of particles is 85.3 g, accounting for 92.32% of the total mass loss in the whole seepage process. With the emission of particles gathered in the outlet area in the slow seepage stage, the pores between the skeleton particles gradually increase and the particle loss speed and amount suddenly change, forming a relatively through seepage channel. This stage is the main stage of particle loss in the whole seepage process. In fact, the seepage volume increases and the water quality is turbid. In the third stage (stable seepage stage, 0.8–1 s), the total mass loss of particles in this stage is 2.1 g, accounting for 2.27% of the total mass loss in the whole seepage stage. As most of the filling particles and some of the skeleton particles that are free from the skeleton network have gushed out, only a few particles will slowly gush out after 0.8 s. The remaining filling particles interact with the large skeleton particles to form a new skeleton. The seepage reaches a stable state and forms a smooth seepage channel.

3.3. *Change of Particle Contact Quantity.* In the process of seepage, particles move upward and gush out, because the contact relationship between particles is changing and the

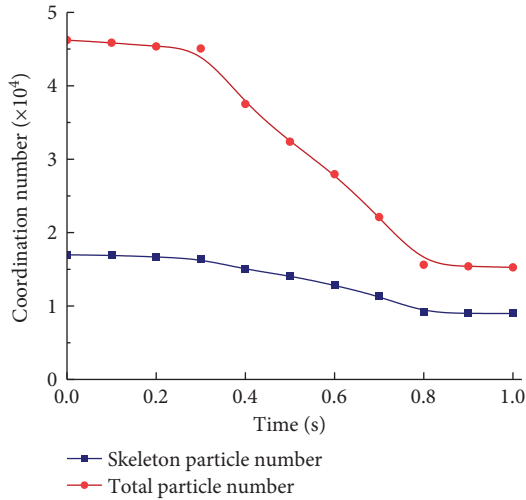


FIGURE 10: Curve of particle coordination number change.

normal contact force and tangential contact force are changing. The contact number between particles is described by the change of coordination number in EDEM with time. The coordination number is greater than the contact number between particles, but the larger the coordination number, the more the contact number between particles. As shown in Figure 10, the particle coordination number versus the time curve is shown. The red curve represents the change of total coordination number between particles, and the blue curve represents the change in coordination number of skeleton particles.

Within 0–0.3 s, the coordination number of skeleton particles did not change much, while the total coordination number of particles decreased slightly to a certain extent. After 0.3 s, the coordination number of skeleton particles began to decrease because the continuous loss of filling particles led to the change of contact force on skeleton particles under the action of seepage force, which made skeleton particles free from the skeleton network move. However, the contact relationship between the skeleton particles in the skeleton network has not changed.

The change of contact quantity between particles is consistent with the seepage stage, and the decrease rate of contact quantity between particles is relatively slow in the process of slow seepage. In the stage of sudden seepage, the contact quantity between filling particles and between filling particles and skeleton particles changes abruptly. During the steady seepage stage, the contact quantity between particles reaches a steady state. After the seepage process, the particles in the model are basically in a stable state, and only a small number of particles will continue to lose. Therefore, the contact number between particles will not change significantly.

3.4. Change of the Porosity. The increasing porosity in the process of seepage is the fundamental reason for the formation of water inrush channels. Because the particle loss in the inlet area is smaller than the total loss, the porosity changes in the inlet area and the total are studied,

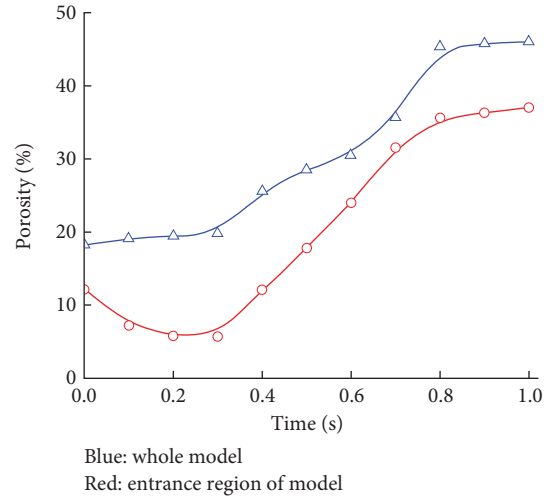


FIGURE 11: Variation curve of porosity with time.

respectively. By adding “Geometry Bin” in EDEM post-processing, the change of porosity in the inlet area is analyzed, where the size is set to 40 mm × 40 mm × 50 mm. The evolution curve of porosity with time cannot be directly generated by EDEM. Therefore, the change of porosity is calculated through the change of particle volume or mass in the region. The calculation is shown as follows:

$$P = \left(1 - \frac{\rho_0}{\rho_s}\right) \times 100\% = \left[1 - \frac{m_s}{\rho_s V}\right] \times 100\%, \quad (2)$$

where P is the porosity, V is the total volume of the model, m_s is the particle mass in the model, ρ_0 is the bulk density of the material, and ρ_s is the material density.

Figure 11 (red curve) shows that the porosity in the entrance region decreases first and then increases rapidly and finally becomes stable with time. In the stage of slow seepage, the hydraulic gradient is relatively small. For larger particles in the outlet area, gravity plays a leading role. Under the downward condition of the resultant force, it moves slowly downward and continuously flows into the “Geometry Bin.” Therefore, in this stage of seepage, the porosity in the inlet area decreases. As the hydraulic gradient reaches the critical hydraulic gradient and enters the sudden seepage stage, the filling particles in the inlet area will move upward rapidly under the drag force of water flow, so the porosity will increase rapidly. After entering the stable seepage stage, there is still a small amount of filling particles moving to the outlet area, but most of the particles have been in a relatively stable state, so the porosity will slowly increase and tend to be stable.

For the overall porosity, the porosity versus time curve (Figure 11, blue curve) can be obtained according to Figure 8. The change of overall porosity is a direct manifestation of particle loss. The time change curve of overall porosity is consistent with the time change curve of lost particle mass in Figure 9. In the slow seepage stage, because a small amount of particles gush out, the overall porosity increases slowly. In the stage of sudden seepage, the hydraulic gradient reaches the critical hydraulic gradient and the overall porosity

increases rapidly with the large amount of particles gushing out. After reaching the stable seepage stage, as the particles have basically remained stable, the overall porosity of the model also tends to be stable.

4. Conclusions

In the process of seepage, the particles will migrate under the action of the flow seepage force and the particles in the outlet area will move before the particles in the inlet area. As the particles in the outlet area gush out, the particles in the inlet area will move and gush out, forming a relatively smooth water inrush channel. Under the condition of variable hydraulic gradient, based on the loss speed and quality of particles, the whole seepage process can be divided into three stages: slow seepage stage, sudden seepage stage, and stable seepage stage. There are critical hydraulic gradients in the slow seepage stage and sudden seepage stage.

The particle loss speed is slow under the condition of the low hydraulic gradient. After reaching the critical hydraulic gradient, the particle loss speed increases significantly. After most of the filling particles gush out, the particle loss speed slows down and tends to be stable. In the process of water inrush, the overall movement trend of particles can be roughly predicted, but the movement trajectory of a single particle is irregular.

The change of contact quantity is mainly caused by the loss of filling particles. The change trend of contact quantity between particles is basically consistent with the change in particle loss quality. In the stage of slow seepage, the contact quantity between particles decreases slowly. The contact quantity between particles decreases rapidly after entering the stage of sudden seepage. In the steady seepage stage, the contact quantity between particles is basically in a stable state.

Data Availability

The original contributions presented in the study are included in the article, and further inquiries can be directed to the corresponding author.

Conflicts of Interest

The author WC is employed by Beijing Guodaotong Highway Design and Research Institute Co., Ltd. The authors YW, FH, and PZ are employed by Beijing Uni.-Construction Group Co., Ltd. The remaining authors declare that they have no conflicts of interest.

Authors' Contributions

The main contribution of SS in this paper is methodology, and the other authors (WC, YW, FH, and PZ) contributed to investigation and analysis.

Acknowledgments

This research was funded by the Beijing Natural Science Foundation (8222023).

References

- [1] Y. Zhao, P. Li, and S. Tian, "Prevention and treatment technologies of railway tunnel water inrush and mud gushing in China," *Journal of Rock Mechanics and Geotechnical Engineering*, vol. 5, no. 6, pp. 468–477, 2013.
- [2] D. Ma, H. Duan, X. Li, Z. Li, Z. Zhou, and T. Li, "Effects of seepage-induced erosion on nonlinear hydraulic properties of broken red sandstones," *Tunnelling and Underground Space Technology*, vol. 91, Article ID 102993, 2019.
- [3] Z. Huang, W. Zeng, Y. Wu, S. Li, and K. Zhao, "Experimental investigation of fracture propagation and inrush characteristics in tunnel construction," *Natural Hazards*, vol. 97, no. 1, pp. 193–210, 2019.
- [4] W. Zeng, Z. Huang, Y. Wu, S. Li, R. Zhang, and K. Zhao, "Experimental investigation on mining-induced strain and failure characteristics of rock masses of mine floor," *Geomatics, Natural Hazards and Risk*, vol. 11, no. 1, pp. 491–509, 2020.
- [5] C. Zou, J. A. Moore, M. Sanayei, Z. Tao, and Y. Wang, "Impedance model of train-induced vibration transmission across a transfer structure into an over track building in a metro depot," *Journal of Structural Engineering*, vol. 148, no. 11, 2022.
- [6] L. Li, S. Sun, J. Wang, W. Yang, S. Song, and Z. Fang, "Experimental study of the precursor information of the water inrush in shield tunnels due to the proximity of a water-filled cave," *International Journal of Rock Mechanics and Mining Sciences*, vol. 130, Article ID 104320, 2020.
- [7] C. Roques, L. Aquilina, O. Bour et al., "Groundwater sources and geochemical processes in a crystalline fault aquifer," *Journal of Hydrology*, vol. 519, pp. 3110–3128, 2014.
- [8] Z. Huang, W. Zeng, and K. Zhao, "Experimental investigation of the variations in hydraulic properties of a fault zone in Western Shandong, China," *Journal of Hydrology*, vol. 574, pp. 822–835, 2019.
- [9] H. Jin, J. Su, and C. Zhao, "Relationship between invert-filling disengaging and deformation of shield tunnel using staggered assembled segment," *KSCE Journal of Civil Engineering*, vol. 26, no. 4, pp. 1966–1977, 2022.
- [10] M. Ma, M. Li, X. Qu, and H. Zhang, "Effect of passing metro trains on uncertainty of vibration source intensity: monitoring tests," *Measurement*, vol. 193, Article ID 110992, 2022.
- [11] X. Wang, S. Li, Z. Xu, J. Hu, D. Pan, and Y. Xue, "Risk assessment of water inrush in karst tunnels excavation based on normal cloud model," *Bulletin of Engineering Geology and the Environment*, vol. 78, no. 5, pp. 3783–3798, 2019.
- [12] F. Qian, "Mechanism analysis and treatment technology of gushing water in Guanjiao tunnel," *Railway Engineering*, vol. 10, pp. 52–58, 2014.
- [13] Y. Ma, J. Yang, L. Li, and Y. Li, "Analysis on ultimate water pressure and treatment measures of tunnels operating in water rich areas based on water hazard investigation," *Alexandria Engineering Journal*, vol. 61, no. 8, pp. 6581–6589, 2022.
- [14] Y. Jiang, P. Zhou, F. Zhou et al., "Failure analysis and control measures for tunnel faces in water-rich sandy dolomite formations," *Engineering Failure Analysis*, vol. 138, Article ID 106350, 2022.
- [15] X. Li, P. Zhang, Z. He, Z. Huang, M. Cheng, and L. Guo, "Identification of geological structure which induced heavy water and mud inrush in tunnel excavation: a case study on Lingjiao tunnel," *Tunnelling and Underground Space Technology*, vol. 69, pp. 203–208, 2017.

- [16] J. Q. Guo, L. W. Ren, and X. L. Liu, "Study on safe thickness of comparatively intact rock ahead of karst tunnel face," *Applied Mechanics and Materials*, vol. 90-93, pp. 2456-2459, 2011.
- [17] S. Jiang, Y. Wang, X. Li, and N. Zhou, "3D numerical simulation for predicting water inflow volume in deep and long tunnels," *Modern Tunnelling Technology*, vol. 379, pp. 78-83, 2016.
- [18] R. Li, "Analysis and treatment measures of pouring water in Cenxi large highway tunnel," *Bridge and Tunnel Engineering*, vol. 90, pp. 33-37, 2013.
- [19] X. Zhao and X. Yang, "Experimental study on water inflow characteristics of tunnel in the fault fracture zone," *Arabian Journal of Geosciences*, vol. 12, no. 13, p. 399, 2019.
- [20] M. Liu and Z. Zhang, "Smoothed particle hydrodynamics (SPH) for modeling fluid-structure interactions," *Science China Physics, Mechanics & Astronomy*, vol. 62, Article ID 984701, 2019.
- [21] B. Bai, D. Rao, T. Xu, and P. Chen, "SPH-FDM boundary for the analysis of thermal process in homogeneous media with a discontinuous interface," *International Journal of Heat and Mass Transfer*, vol. 117, pp. 517-526, 2018.
- [22] B. Bai, F. Long, D. Rao, and T. Xu, "The effect of temperature on the seepage transport of suspended particles in a porous medium," *Hydrological Processes*, vol. 31, no. 2, pp. 382-393, 2017.
- [23] W. C. Cheng, X. D. Bai, B. B. Sheil, G. Li, and F. Wang, "Identifying characteristics of pipejacking parameters to assess geological conditions using optimisation algorithm-based support vector machines," *Tunnelling and Underground Space Technology*, vol. 106, Article ID 103592, 2020.
- [24] B. Bai, "Fluctuation responses of saturated porous media subjected to cyclic thermal loading," *Computers and Geotechnics*, vol. 33, no. 8, pp. 396-403, 2006.
- [25] B. Yuan, Z. Li, W. Chen et al., "Influence of groundwater depth on pile-soil mechanical properties and fractal characteristics under cyclic loading," *Fractal and Fractional*, vol. 6, no. 4, p. 198, 2022.
- [26] B. Bai, G. C. Yang, T. Li, and G. S. Yang, "A thermodynamic constitutive model with temperature effect based on particle rearrangement for geomaterials," *Mechanics of Materials*, vol. 139, Article ID 103180, 2019.
- [27] B. Bai, R. Zhou, G. Cai, W. Hu, and G. Yang, "Coupled thermo-hydro-mechanical mechanism in view of the soil particle rearrangement of granular thermodynamics," *Computers and Geotechnics*, vol. 137, Article ID 104272, 2021.
- [28] B. Bai and Z. Su, "Thermal responses of saturated silty clay during repeated heating-cooling processes," *Transport in Porous Media*, vol. 93, pp. 1-11, 2012.
- [29] B. Bai, Q. Nie, Y. Zhang, X. Wang, and W. Hu, "Cotransport of heavy metals and SiO₂ particles at different temperatures by seepage," *Journal of Hydrology*, vol. 597, Article ID 125771, 2021.
- [30] W. Hu, W. C. Cheng, S. Wen, and K. Yuan, "Revealing the enhancement and degradation mechanisms affecting the performance of carbonate precipitation in EICP process," *Frontiers in Bioengineering and Biotechnology*, vol. 9, Article ID 750258, 2021.
- [31] L. Guoyu, Y. Changhong, L. Xiaozhao, J. Jianping, and M. Ji, "Exploration of water resource and multiple model for water resource development in karst areas with the preferred plane theory," *Acta Geologica Sinica - English Edition*, vol. 77, no. 1, pp. 129-135, 2010.
- [32] B. Bai and T. Li, "Irreversible consolidation problem of a saturated porothermoelastic spherical body with a spherical cavity," *Applied Mathematical Modelling*, vol. 37, no. 4, pp. 1973-1982, 2013.
- [33] B. Bai, L. Guo, and S. Han, "Pore pressure and consolidation of saturated silty clay induced by progressively heating/cooling," *Mechanics of Materials*, vol. 75, pp. 84-94, 2014.
- [34] B. Yuan, M. Chen, W. Chen, Q. Luo, and H. Li, "Effect of pile-soil relative stiffness on deformation characteristics of the laterally loaded pile," *Advances in Materials Science and Engineering*, vol. 13, p. 1, 2022.
- [35] B. Yuan, W. Chen, J. Zhao, F. Yang, Q. Luo, and T. Chen, "The effect of organic and inorganic modifiers on the physical properties of granite residual soil," *Advances in Materials Science and Engineering*, vol. 13, p. 1, 2022.
- [36] Z. Zhou, L. Li, S. Shi et al., "Study on tunnel water inrush mechanism and simulation of seepage failure process," *Rock and Soil Mechanics*, vol. 41, pp. 3621-3631, 2020.
- [37] Y. Wang, F. Geng, S. Yang, H. Jing, and B. Meng, "Numerical simulation of particle migration from crushed sandstones during groundwater inrush," *Journal of Hazardous Materials*, vol. 362, pp. 327-335, 2019.
- [38] Z. Xu, M. Xian, X. Li, and W. Zhou, "Risk assessment of water inrush in shallow karst tunnel with stable surface water supply: case study," *Geomechanics and Engineering*, vol. 25, pp. 495-508, 2021.
- [39] X. Chen and R. Lyu, "Experimental study on effects of particle migration on hydraulic Characteristics of crushed sandstone during water inrush," *China Mining Magazine*, vol. 30, pp. 184-188, 2021.
- [40] M. Wang, W. Yang, Z. Zhou et al., "Experimental research on the effect of particle migration of a filling medium in a fault during water and mud inrush," *Arabian Journal of Geosciences*, vol. 14, no. 21, p. 2206, 2021.
- [41] B. Bai, T. Xu, Q. Nie, and P. Li, "Temperature-driven migration of heavy metal Pb²⁺ along with moisture movement in unsaturated soils," *International Journal of Heat and Mass Transfer*, vol. 153, Article ID 119573, 2020.
- [42] J. Kozicki and F. V. Donzé, "A new open-source software developed for numerical simulations using discrete modeling methods," *Computer Methods in Applied Mechanics and Engineering*, vol. 197, no. 49-50, pp. 4429-4443, 2008.
- [43] B. Bai, S. Jiang, L. Liu, X. Li, and H. Wu, "The transport of silica powders and lead ions under unsteady flow and variable injection concentrations," *Powder Technology*, vol. 387, pp. 22-30, 2021.
- [44] B. Bai, Q. Nie, H. Wu, and J. Hou, "The attachment-detachment mechanism of ionic/nanoscale/microscale substances on quartz sand in water," *Powder Technology*, vol. 394, pp. 1158-1168, 2021.
- [45] W. Hu, W. C. Cheng, S. Wen, and M. Mizanur Rahman, "Effects of chemical contamination on microscale structural characteristics of intact loess and resultant macroscale mechanical properties," *Catena*, vol. 203, Article ID 105361, 2021.
- [46] Z. F. Xue, W.-C. Cheng, L. Wang, and G. Song, "Improvement of the shearing behaviour of loess using recycled straw fiber reinforcement," *KSCE Journal of Civil Engineering*, vol. 25, no. 9, pp. 3319-3335, 2021.
- [47] H. Jin, Q. Tian, and Z. Li, "Crack development of rebar rust in rubberized concrete using mesoscale model," *Construction and Building Materials*, vol. 321, Article ID 126409, 2022.

- [48] Z. F. Xue, W. C. Cheng, L. Wang, and W. Hu, "Effects of bacterial inoculation and calcium source on microbial-induced carbonate precipitation for lead remediation," *Journal of Hazardous Materials*, vol. 426, Article ID 128090, 2022.
- [49] L. Xu and M. Ma, "Dynamic response of the multilayered half-space medium due to the spatially periodic harmonic moving load," *Soil Dynamics and Earthquake Engineering*, vol. 157, Article ID 107246, 2022.
- [50] S. Shi, X. Xie, L. Bu, L. Li, and Z. Zhou, "Hazard-based evaluation model of water inrush disaster sources in karst tunnels and its engineering application," *Environmental Earth Sciences*, vol. 77, no. 4, p. 141, 2018.